

## Quasi-Vertical Profiles—A New Way to Look at Polarimetric Radar Data

ALEXANDER RYZHKOV, PENGFEI ZHANG, AND HEATHER REEVES

*Cooperative Institute for Mesoscale Meteorological Studies, University of Oklahoma,  
and NOAA/OAR/National Severe Storms Laboratory, Norman, Oklahoma*

MATTHEW KUMJIAN

*The Pennsylvania State University, University Park, Pennsylvania*

TIMO TSCHALLENGER, SILKE TRÖMEL, AND CLEMENS SIMMER

*Meteorological Institute, University of Bonn, Bonn, Germany*

(Manuscript received 22 January 2015, in final form 26 December 2015)

### ABSTRACT

A novel methodology is introduced for processing and presenting polarimetric data collected by weather surveillance radars. It involves azimuthal averaging of radar reflectivity  $Z$ , differential reflectivity  $Z_{DR}$ , cross-correlation coefficient  $\rho_{hv}$ , and differential phase  $\Phi_{DP}$  at high antenna elevation, and presenting resulting quasi-vertical profiles (QVPs) in a height-versus-time format. Multiple examples of QVPs retrieved from the data collected by S-, C-, and X-band dual-polarization radars at elevations ranging from  $6.4^\circ$  to  $28^\circ$  illustrate advantages of the QVP technique. The benefits include an ability to examine the temporal evolution of microphysical processes governing precipitation production and to compare polarimetric data obtained from the scanning surveillance weather radars with observations made by vertically looking remote sensors, such as wind profilers, lidars, radiometers, cloud radars, and radars operating on spaceborne and airborne platforms. Continuous monitoring of the melting layer and the layer of dendritic growth with high vertical resolution, and the possible opportunity to discriminate between the processes of snow aggregation and riming, constitute other potential benefits of the suggested methodology.

### 1. Introduction

Polarimetric radars provide unique insight into microphysical processes in clouds and precipitation. This knowledge will create opportunities for better microphysical parameterizations in numerical weather prediction (NWP) models and for assimilation of dual-polarization data into storm-scale models. Different microphysical processes (size sorting, evaporation, melting, freezing, riming, aggregation, diffusional growth, etc.) are characterized by specific “polarimetric fingerprints” (e.g., Kumjian 2012). These can be used to evaluate and eventually improve the models via converting their outputs into fields of polarimetric radar variables and adjusting parameterizations in a way that

the observed polarimetric fingerprints are adequately reproduced.

The routine presentation of radar data in the plan position indicator (PPI) mode is not convenient for linking polarimetric radar signatures aloft, associated microphysical processes, and precipitation near the surface. Most convenient for the latter are scans along vertical planes in the so-called range–height indicator (RHI) mode; however, such scans typically are not available from operational systems due to time constraints. In principle, vertical cross sections of different radar variables can be obtained from a series of PPIs at different elevations (i.e., reconstructed RHIs), but their quality and vertical resolution are usually worse than that of “genuine” RHIs. On the other hand, genuine RHIs yield information only in selected azimuthal directions and thus do not represent the general structure of the storm or its evolution.

To get a better understanding of the microphysical processes that govern precipitation generation and evolution, it is beneficial to complement polarimetric

---

*Corresponding author address:* Alexander Ryzhkov, CIMMS, University of Oklahoma, 120 David L. Boren Blvd., Ste. 2100, Norman, OK 73072.  
E-mail: alexander.ryzhkov@noaa.gov

scanning radar measurements with multifrequency observations by other remote sensors, such as wind profilers, cloud radars, spaceborne or airborne radars, lidars, and radiometers—all of which are mostly vertically pointing. Observations from these instruments are usually presented in a height-versus-time format. Polarimetric weather radars, however, are rarely used to probe the atmosphere in the vertical direction because key polarimetric variables, including differential reflectivity  $Z_{DR}$ , total differential phase  $\Phi_{DP}$ , and specific differential phase  $K_{DP}$ , exploit the signals produced by preferentially horizontally aligned nonspherical hydrometeors. These require antenna elevations, say, below  $20^{\circ}$ – $30^{\circ}$  to capitalize on the contrasts between orthogonally polarized components of the radar returns. One exception is the common practice to use vertical soundings for the absolute calibration of  $Z_{DR}$ . Some operational polarimetric radars, such as the U.S. WSR-88Ds, cannot even look vertically due to antenna mechanical constraints. The area-covering scanning strategies of weather radars and the usual vertical scanning modes of other atmospheric remote sensing instruments might contribute to the current lack of multiplatform, synergistic observational studies.

Dwell times adopted for the scanning strategies of operational radars are usually quite short (typically about 50 ms for operational WSR-88D radars). Such short dwell times often result in significant statistical errors in estimates of the polarimetric radar variables, especially in areas characterized by low cross-correlation coefficients  $\rho_{hv}$ , the magnitude of which determines the statistical accuracy of radar moment estimates. The magnitude of  $\rho_{hv}$  is particularly low in the melting layer of stratiform clouds and, as a result, the key polarimetric variables  $Z_{DR}$ ,  $\Phi_{DP}$ , and  $\rho_{hv}$  are usually quite noisy there. For a long time, the noisiness of  $\Phi_{DP}$  in the melting layer has impeded the separation of the contributions of the forward scattering associated with  $K_{DP}$  and the backscattering related to the backscatter differential phase  $\delta$  to total  $\Phi_{DP}$ . The enhanced backscatter differential phase shows up as a “bump” in the slant profiles of  $\Phi_{DP}$ , which usually monotonically increases with range with the slope determined by  $K_{DP}$ . The quantity  $\delta$  characterizes local scattering properties of hydrometeors in the radar resolution volume, such as non-Rayleigh or resonance scattering, by large hydrometeors. In contrast,  $K_{DP}$  characterizes the cumulative differential phase shift attributed to the propagation of electromagnetic wave through the medium filled with nonspherical particles. To reduce the noisiness of the differential phase within the melting layer, Trömel et al. (2013, 2014) suggest azimuthal averaging at high antenna elevation angles for the estimation of  $\delta$ . Similarly, Kumjian et al. (2013) recommended

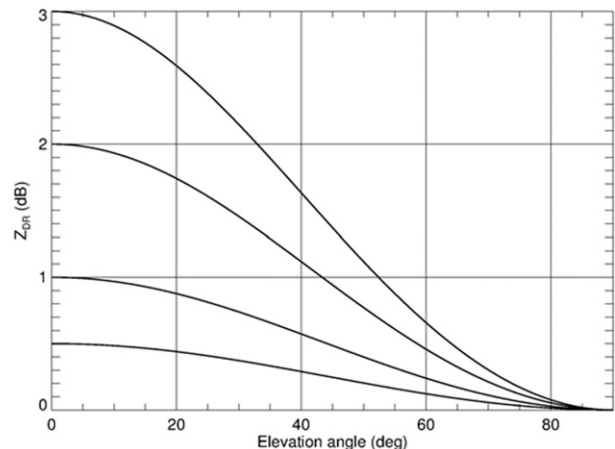


FIG. 1. Dependence of the  $Z_{DR}$  of oblate spheroidal hydrometeors on elevation angle for different values of intrinsic  $Z_{DR}$  at zero elevation angle.

such azimuthal averaging to quantify rather small enhancements of  $Z_{DR}$  and  $K_{DP}$  within the layer of melted hydrometeors freezing into ice pellets.

In this study, we follow a similar approach and routinely obtain the so-called high-resolution quasi-vertical profiles (QVPs) of  $Z$ ,  $Z_{DR}$ ,  $\rho_{hv}$ , and  $\Phi_{DP}$  at relatively high elevation angles. We represent these profiles in a time-versus-height format to investigate the temporal evolution of key microphysical processes in clouds and precipitation.

## 2. QVP methodology

The QVPs of the polarimetric radar variables are obtained by azimuthal averaging of the radar data collected during standard conical scans at antenna elevation angles exceeding  $10^{\circ}$ – $20^{\circ}$ . Such high elevations minimize the effects of radar beam broadening and horizontal inhomogeneity. The values of  $Z_{DR}$ ,  $\Phi_{DP}$ , and  $K_{DP}$  generally decrease only slightly with increasing elevation if the elevation angle remains below  $20^{\circ}$ – $30^{\circ}$ . Theoretical dependencies of  $Z_{DR}$  on elevation angles for oblate spheroidal hydrometeors described by the formula (Ryzhkov et al. 2005)

$$Z_{dr}(\theta) \approx \frac{Z_{dr}(0)}{[Z_{dr}^{1/2}(0) \sin^2 \theta + \cos^2 \theta]^2} \quad (1)$$

are illustrated in Fig. 1. In Eq. (1), linear scale  $Z_{dr}(0)$  and  $Z_{dr}(\theta)$  are the differential reflectivities at elevation angles  $0^{\circ}$  and  $\theta^{\circ}$ , respectively. If  $Z_{DR}$  (expressed in log scale) at grazing angles is below 1 dB, then it decreases by less than 0.15 dB at an elevation of  $20^{\circ}$ , which is within common measurement error of  $Z_{DR}$  (0.1–0.2 dB). For higher values of  $Z_{DR}$  and higher elevations, Eq. (1)

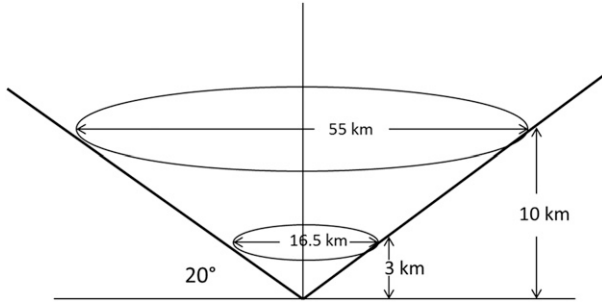


FIG. 2. Conical volume representing azimuthally averaged quasi-vertical profiles of radar variables.

and Fig. 1 can be used for calculating the equivalent value of  $Z_{DR}$  at  $0^\circ$  elevation [ $Z_{DR}(0)$ ].

Azimuthal averaging reduces the statistical errors of the radar estimates without compromising temporal resolution and assigns their average vertical profiles to a conical volume with a vertical axis (Fig. 2). The standard deviations of the  $\Phi_{DP}$  and  $Z_{DR}$  estimates are given by the following formulas (Melnikov 2004):

$$SD(\Phi_{DP}) = 30.3 \left( \frac{\rho_{hv}^{-2} - 1}{\sigma_{vn} M} \right)^{1/2} \quad (2)$$

and

$$SD(Z_{DR}) = 4.62 \left( \frac{1 - \rho_{hv}^2}{\sigma_{vn} M} \right)^{1/2}, \quad (3)$$

where

$$\sigma_{vn} = 4\sigma_v T/\lambda, \quad (4)$$

$M$  is the number of samples,  $\sigma_v$  is the Doppler spectrum width,  $T$  is the pulse repetition period (PRT), and  $\lambda$  is the radar wavelength. For S-band WSR-88D radars operating with  $T = 3.1 \times 10^{-3}$  s (long PRT) and  $M = 16$  in the surveillance scan mode (Ice et al. 2013) and for a typical value of  $\sigma_v = 3 \text{ ms}^{-1}$ , the magnitudes of  $SD(\Phi_{DP})$  and  $SD(Z_{DR})$  measured within the melting layer with  $\rho_{hv} = 0.94$  are  $4.73^\circ$  and  $0.68 \text{ dB}$ , respectively. If the melting layer is horizontally uniform, then azimuthal averaging of  $\Phi_{DP}$  and  $Z_{DR}$  over 360 azimuths would result in the statistical error reduction by a factor of  $360^{1/2}$ , which yields standard deviations of azimuthally averaged estimates as low as  $0.25^\circ$  and  $0.036 \text{ dB}$  for  $\Phi_{DP}$  and  $Z_{DR}$ , respectively. These errors are even smaller outside the melting layer, where the cross-correlation coefficient is usually higher than 0.94.

If the cloud is not horizontally uniform within the cone, then the errors of the azimuthally averaged estimates are larger, but a significant reduction in the statistical

uncertainty compared to the case of a single radial still remains. For an antenna elevation of  $20^\circ$ , the diameter of the circle encompassing the averaging area increases from 16.5 km at a height of 3 km (the frequently observed height of the melting layer; see Fig. 2) to 55 km at a height of 10 km. The varying diameter of the averaging circle has to be taken into account in the interpretation of the QVP data.

According to the initial version of the QVP methodology, only the gates with  $\rho_{hv} > 0.6$  and  $Z > -10 \text{ dBZ}$  are used for azimuthal averaging and the number of valid gates (or azimuths) along the circle should exceed 30 in order to make an estimate of the QVP variable. Such averaging is performed at every radial gate with a typical slant range resolution  $\Delta r$  of 250 m. The resulting vertical resolution of the QVP data is determined by two factors: the size of radial range gate  $\Delta r$  and the width of the radar beam  $r\Delta\theta$ , where  $r$  is the slant range and  $\Delta\theta$  is the antenna beamwidth. Therefore, effective vertical resolution of QVP can be roughly estimated as the larger of the two terms:

$$\Delta h_1 = \Delta r \sin \alpha \quad (5)$$

and

$$\Delta h_2 = h\Delta\theta \cot \alpha, \quad (6)$$

where  $\alpha$  is the antenna elevation angle and  $h$  is the height above ground. The term (5) increases with increasing  $\alpha$ , whereas Eq. (6) decreases with higher antenna elevations. For  $\alpha = 20^\circ$ ,  $\Delta r = 0.25 \text{ km}$ , and  $\Delta\theta = 1^\circ$ ,  $\Delta h_2$  exceeds  $\Delta h_1$  if  $h > 1.78 \text{ km}$ ; that is, the beam broadening term becomes dominant at higher altitudes. The corresponding vertical resolution determined by the term  $\Delta h_2$  is about 100 m at  $h = 2 \text{ km}$  and 400 m at  $h = 8 \text{ km}$  for  $\alpha = 20^\circ$ . The vertical resolution degrades with decreasing antenna elevation proportionally to  $\cot \alpha$ . Nevertheless, it remains much better than the one yielded by RHI reconstructed from the series of PPI scans as will be shown in the next section.

Any horizontal heterogeneity of the storm introduces the uncertainty in the QVPs. The measure of “tolerable” heterogeneity is difficult to quantify and further investigation is needed. The initial QVP methodology will be modified in the course of its future exploration using extended datasets. Possible refinements may include separation of the stratiform and convective echo to avoid contamination from spatially nonuniform convective elements. Another possibility is to utilize multiple (but relatively close) elevations to further reduce the statistical uncertainty as was done by Giangrande et al. (2008) for polarimetric detection of the melting layer.

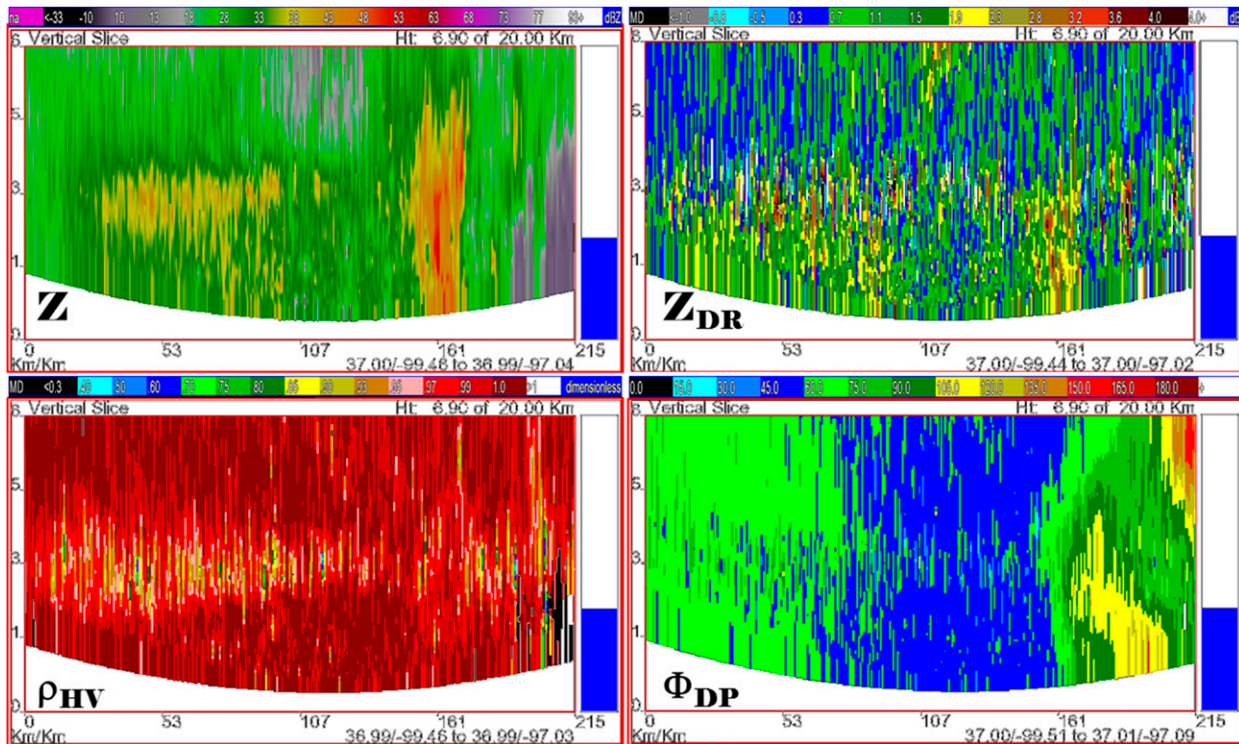


FIG. 3. Reconstructed composite RHIs of  $Z$ ,  $Z_{DR}$ ,  $\rho_{hv}$ , and  $\Phi_{DP}$  measured by the KVNx WSR-88D radar in the case of an MCS observed in northern Oklahoma on 20 May 2011.

### 3. QVP examples at S, C, and X bands

The advantages of the QVP methodology are first demonstrated using polarimetric data collected by the KVNx WSR-88D radar (Vance Air Force Base, Oklahoma), for a mesoscale convective system (MCS) observed in northern Oklahoma on 20 May 2011, during the Midlatitude Continental Convective Clouds Experiment (MC3E). Typical reconstructed RHIs of  $Z$ ,  $Z_{DR}$ , and  $\rho_{hv}$  are shown in Fig. 3. The  $\rho_{hv}$  depression and  $Z_{DR}$  enhancement are visible in the melting layer of the stratiform part of the MCS, but the polarimetric data assembled in the reconstructed RHI format are quite noisy and have low native spatial resolution. The same radar data are utilized for generating the quasi-vertical profiles from the  $19.5^\circ$  elevation angle (the highest antenna elevation in the standard WSR-88D scanning strategy). The QVPs are presented in Fig. 4 in a time-versus-height format for the period 1000–1200 UTC, which spans 28 standard volume scans updated every 5 min. Figure 4 illustrates the evolution of the stratiform part of the MCS as it passed over the radar with high vertical resolution. At about 1100 UTC (i.e., in the middle of the observation period), the melting-layer signature is characterized by  $Z$  exceeding 42 dBZ,  $Z_{DR}$  exceeding 2 dB at the bottom of the melting layer,  $\rho_{hv}$

reduced down to 0.94, and an extremely high  $\delta$  reaching  $40^\circ$  in the middle of the melting layer (bottom-right panel). This backscatter differential phase in the melting layer is in agreement with similarly high values of  $\delta$  at S band reported by Trömel et al. (2014).

Quasi-vertical profiles have been generated for a number of storms observed with operational WSR-88D radars and research dual-polarization radars operating at C and X bands with overlaid temperature contours retrieved from the regional NWP models. All examples demonstrate obvious benefits of QVPs for various practical applications, which are now discussed.

Figures 5 and 6 show QVPs of  $Z$ ,  $Z_{DR}$ ,  $\rho_{hv}$ , and  $\Phi_{DP}$  generated from the KLWX WSR-88D radar (Sterling, Virginia) data collected throughout Hurricane Sandy at elevations of  $19.5^\circ$  on 29 October and  $9.9^\circ$  on 30 October 2012. Each figure illustrates the QVP evolution during 24 h and reveals the complicated internal structure of the storm. There are abrupt variations of the melting-layer height throughout time, as illustrated by elevated  $Z$ ,  $Z_{DR}$ , and  $\delta$ , and depressed  $\rho_{hv}$ . All four of these variables can be effectively monitored using the height-versus-time format while preserving vertical resolution. One can examine these observations against output from the High-Resolution Rapid Refresh (HRRR) model (Alexander et al. 2010). This model has a grid spacing of 3 km, 51



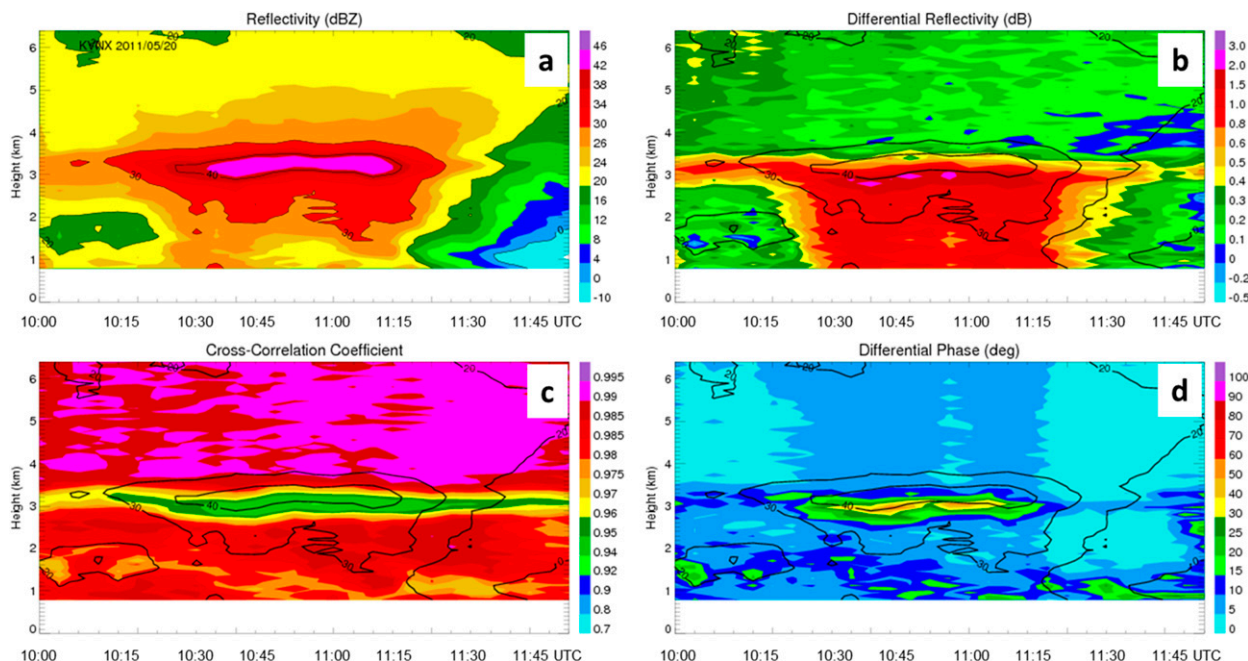


FIG. 4. The height-vs-time representation of quasi-vertical profiles of (a)  $Z$ , (b)  $Z_{DR}$ , (c)  $\rho_{hv}$ , and (d)  $\Phi_{DP}$  retrieved from the KVNIX WSR-88D radar data collected at elevation  $19.5^\circ$  in the case of an MCS observed in northern Oklahoma on 20 May 2011. Overlaid are contours of  $Z$ .

vertical levels, and is updated hourly. Note the abrupt lifting of the melting layer by about 2 km detected by the radar between 2000 and 2400 UTC (Fig. 5) that was not captured by the model (Fig. 7). However, the general trends in the evolution of the height of the melting layer are consistent between the QVP and HRRR, including the drop of the melting layer almost to the surface after the 0800 UTC scan in Fig. 6 during the second day of observations. Note that monitoring the height of the freezing level is critical for timing and spatial variability of surface winter mixed-precipitation types. As in the case of the MCS illustrated in Fig. 4, the values of  $\delta$  within the melting layer vary between  $0^\circ$  and  $40^\circ$ . Trömel et al. (2014) hypothesize that the magnitude of  $\delta$  within the melting layer is determined by the maximal size of snowflakes falling through it. The values of  $\delta$  approaching  $40^\circ$  are indicative of melting snowflakes well exceeding 1 cm.

Other important and persistent features, 2–3 km above the freezing level particularly well displayed in Fig. 5 at times between 1100 and 2300 UTC, are an increase of  $Z_{DR}$  (up to 1.5–2 dB), a reduction of  $\rho_{hv}$ , and a strong vertical gradient of  $Z$ ; these are associated with vigorous dendritic growth and onset of aggregation at temperatures between  $-10^\circ$  and  $-15^\circ\text{C}$  (Kennedy and Rutledge 2011; Ryzhkov et al. 2011; Andrić et al. 2013; Bechini et al. 2013; Thompson et al. 2014; Schrom et al. 2015). The signature strongly varies in time and is

occasionally accompanied by noticeable vertical gradients of  $\Phi_{DP}$  caused by non-zero  $K_{DP}$ . Note that while the backscatter differential phase (which is significant in the melting layer) shows up as a bump in the slant profiles of  $\Phi_{DP}$ , the forward propagation part of  $\Phi_{DP}$  determined by  $K_{DP}$  manifests itself as a monotonic increase of  $\Phi_{DP}$  with height. Interestingly, at certain times, very strong increases of  $K_{DP}$  and  $Z_{DR}$  accompanied by the reduction of  $\rho_{hv}$  are observed near the very top of the cloud, where anisotropic pristine ice crystals are likely generated (e.g., between 1430 and 1630 UTC in Fig. 5) (Kumjian et al. 2014).

The  $Z_{DR}$  decreases and  $Z$  increases below the layer of dendritic growth, which is commonly attributed to aggregation and/or riming. The  $Z_{DR}$  decreases to a few tenths of a decibel just above the level where melting starts. However, this  $Z_{DR}$  reduction occurs at different paces for riming and aggregation, so that  $Z_{DR}$  is generally 0.1–0.3 dB lower just above the freezing level in the case of riming, which makes ice particles more spherical (Vogel et al. 2015; Kumjian et al. 2015, manuscript submitted to *J. Geophys. Res. Atmos.*; Giangrande et al. 2015, manuscript submitted to *J. Geophys. Res. Atmos.*). Such small differences are clearly visible in the QVP time series of  $Z_{DR}$  (Figs. 5 and 6) because azimuthal averaging greatly reduces statistical errors of the  $Z_{DR}$  estimates, allowing for subtle differences to stand out. Other commonly observed manifestations of riming

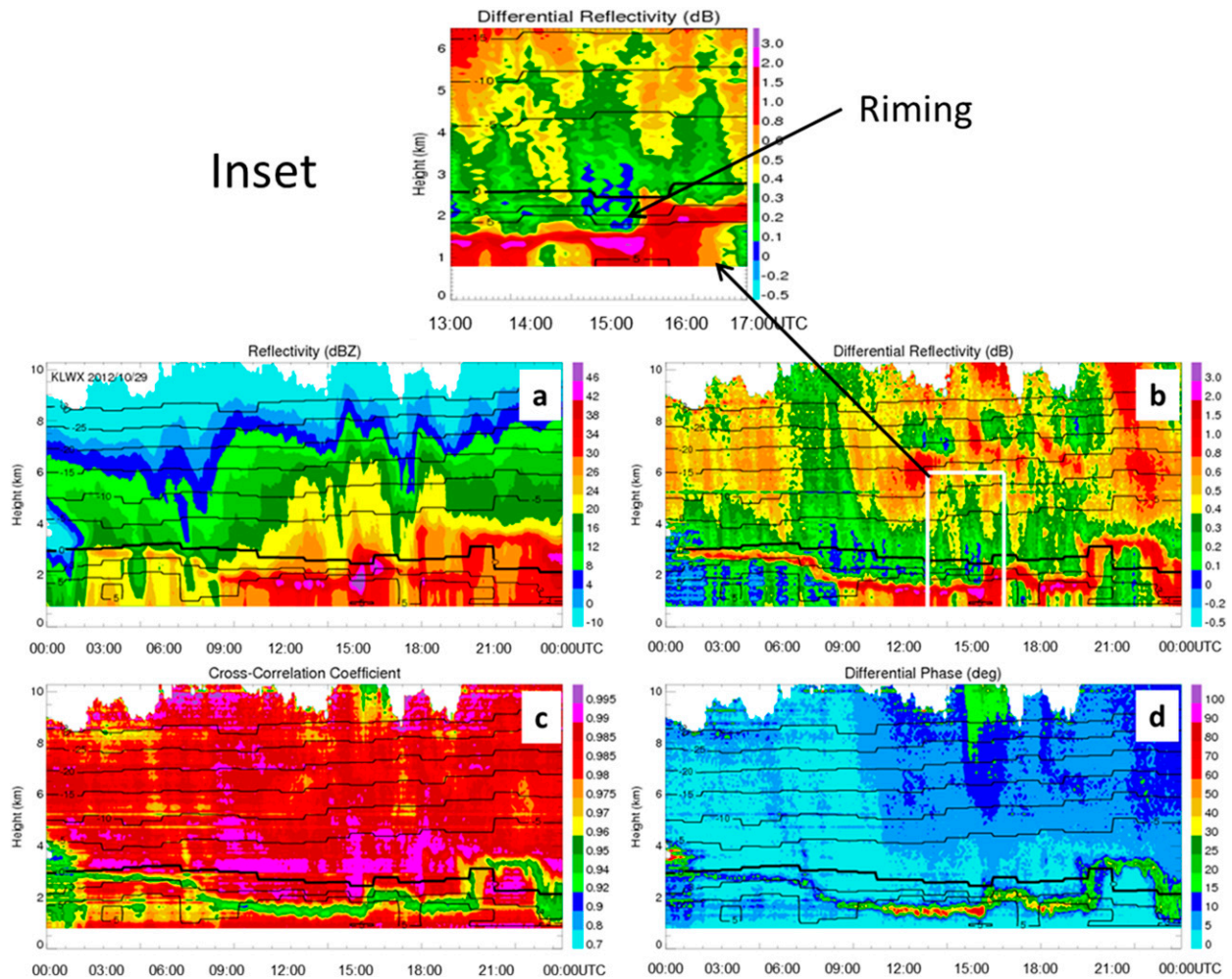


FIG. 5. As in Fig. 4, but for data during Hurricane Sandy on 29 Oct 2012 and with contours of wet-bulb temperature ( $^{\circ}\text{C}$ ) retrieved from the HRRR model. The signature of riming is illustrated in the top panel inset corresponding to the white rectangle in (b).

are the radar reflectivity enhancement and the “sagging” of the melting layer because rimed snow particles have higher density, fall faster, and completely melt at lower altitudes compared to nonrimed snow (Zawadzki et al. 2005; Ryzhkov et al. 2008; Trömel et al. 2014; Kumjian et al. 2015, manuscript submitted to *J. Geophys. Res. Atmos.*). The riming signature is visible during the period between 1440 and 1600 UTC within the height interval from 1.5 to 3.5 km in Fig. 5 (see inset).

The link between downward extension (or sagging) of the melting layer and riming has been confirmed by model simulations (e.g., Zawadzki et al. 2005; Ryzhkov et al. 2008; Trömel et al. 2014; Kumjian et al. 2015, manuscript submitted to *J. Geophys. Res. Atmos.*) and polarimetric radar observations combined with the measurements of vertical velocities by wind profilers (Teshiba et al. 2009) although riming was not explicitly mentioned in the latter study. The association of the

$Z_{\text{DR}}$  depression with riming is less obvious. On the one hand, riming makes ice particles more spherical, which results in the decrease of  $Z_{\text{DR}}$ . On the other hand, increasing snow density caused by riming tends to increase  $Z_{\text{DR}}$ . The fact that all our observations indicate a reduction of  $Z_{\text{DR}}$  in snow aloft during the sagging episodes, points to the fact that the impact of the particle shape is stronger than the impact of density, so that the net effect is the decrease of  $Z_{\text{DR}}$  in the case of heavy riming (see also Vogel et al. 2015).

The QVPs in Figs. 5 and 6 do not reach the surface because the lowest eight 250-m range gates of the WSR-88D radar data are censored out by the signal processor. This is not a problem for grazing angles (i.e., antenna  $< 5^{\circ}$ ) but at higher elevation of  $19.5^{\circ}$  this results in a loss of data within the first 700 m above the surface. This may prevent identification of the time when the melting layer descends to the ground and surface precipitation

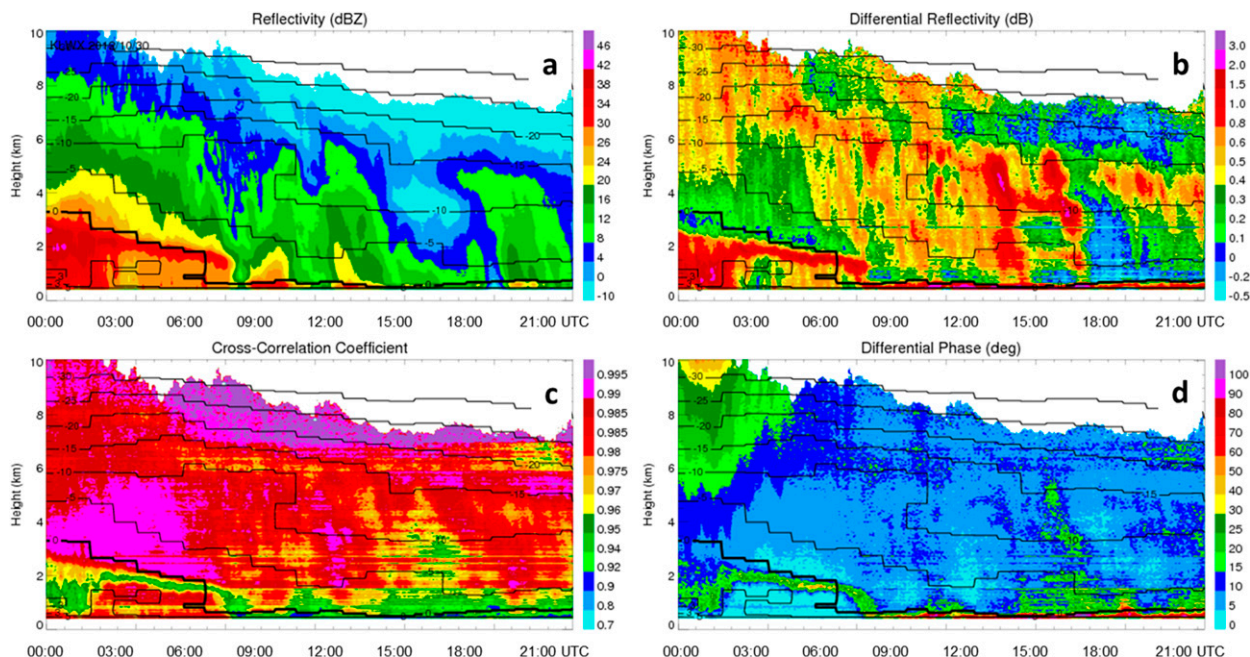


FIG. 6. As in Fig. 5, but for elevation  $9.9^\circ$  during Hurricane Sandy on 30 Oct 2012.

changes to snow at the surface, as in the second day of Hurricane Sandy observations illustrated in Fig. 6. For this reason, the data shown in Fig. 6 were taken from the lower elevation of  $9.9^\circ$  to reduce the depth of the “blank” layer down to 350 m. One has to keep in mind, however, that decreasing antenna elevations degrade the vertical resolution of QVPs (as specified in section 2) and increase the uncertainty associated with azimuthal averaging over larger and potentially more heterogeneous areas of the storm.

Restoring radar data in the first eight range gates would also be beneficial for capturing low-level microphysical processes and signatures, such as the “refreezing signature” described by Kumjian et al. (2013) and Ryzhkov et al. (2014). The refreezing signature is commonly marked by an increase of  $Z_{DR}$  within a narrow layer where supercooled liquid drops freeze to ice pellets so that freezing rain changes to sleet. An example of the refreezing layer at about 500 m above the surface observed by the KTLX WSR-88D radar in Oklahoma City, Oklahoma, is shown in the QVP height–time plot in Fig. 8. The melting layer associated with an elevated temperature inversion between 2 and 3 km is identified by the typical increase of  $Z$ ,  $Z_{DR}$ , and  $\delta$  as well as the drop in  $\rho_{hv}$ . The detection of the refreezing signature becomes possible using the QVP retrieved at elevation  $6.4^\circ$ . The series of vertical profiles of wet-bulb temperature retrieved from the HRRR model (Fig. 9) for this event indicates a classic temperature stratification favorable for a freezing rain–ice pellets transition. A deep,

warm layer lies aloft and a very cold subfreezing layer remains next to the surface around 2100 UTC, when the refreezing signature becomes evident in the QVP. Note that the refreezing signature is often transient and poorly visible at the lowest radar elevations. Hence, the QVP provides a unique opportunity to observe its onset and demise, which has important practical implications for radar classification of winter precipitation types.

The QVP time series can also conveniently be used for continuous monitoring of  $Z_{DR}$  calibration. Ryzhkov et al. (2005) suggested using  $Z_{DR}$  measured in snow just

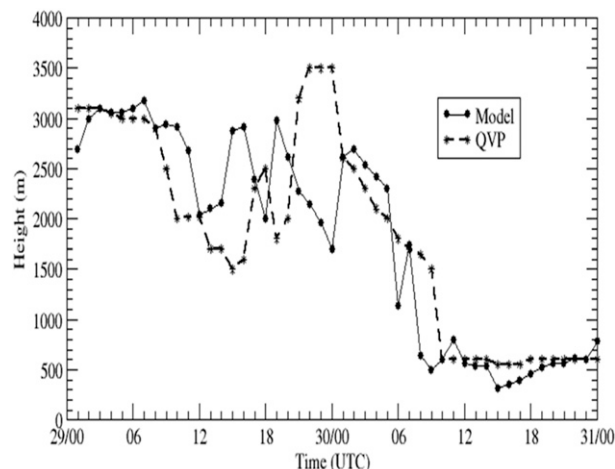


FIG. 7. Temporal evolution of the height of the freezing level retrieved from the HRRR model (solid line) and the KTLX WSR-88D radar (dashed line) during 48 h of the Hurricane Sandy event.



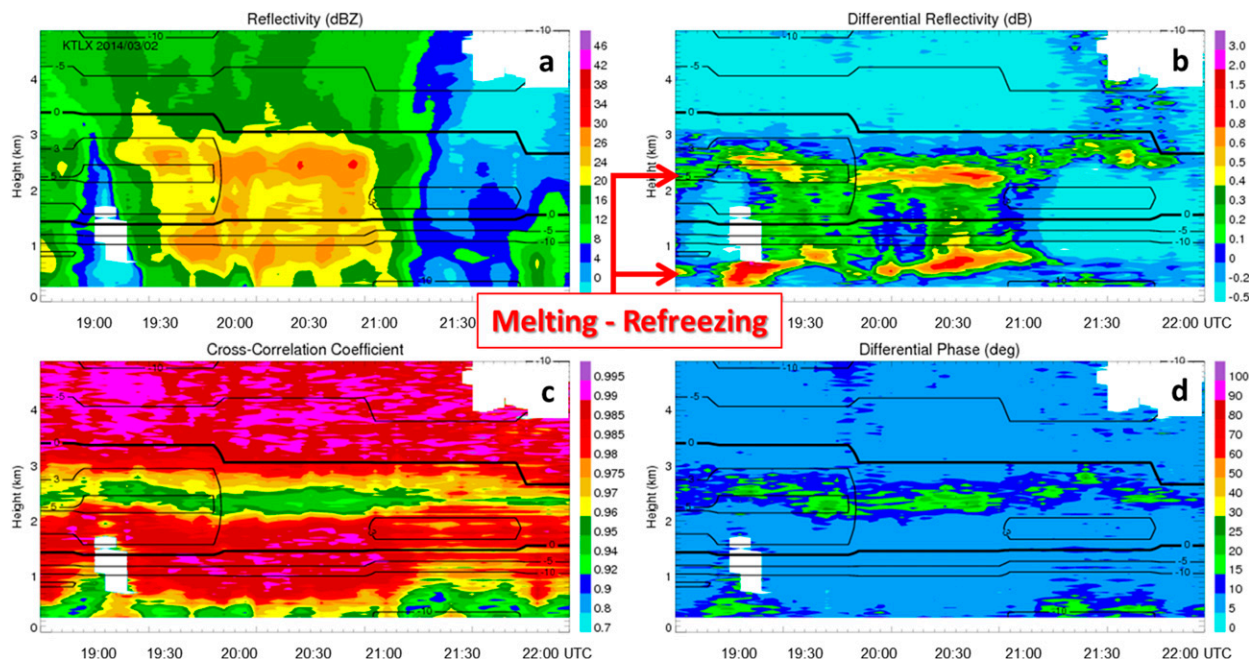


FIG. 8. As in Fig. 4, but for data collected at elevation  $6.4^\circ$  during the freezing rain event in central Oklahoma on 2 Mar 2014. The layers of enhanced differential reflectivity indicating the melting and refreezing layers are shown by arrows in (b).

above the freezing level for absolute calibration of differential reflectivity because the intrinsic  $Z_{DR}$  in heavily aggregated dry snow is less than 0.25 dB and does not vary much. We assume that the  $Z_{DR}$  of dry aggregated snow is slightly positive, whereas most of rimed snow has a  $Z_{DR}$  very close to zero (especially if a higher antenna elevation is used). This was confirmed in the recent studies by Vogel et al. (2015), Kumjian et al. (2015, manuscript submitted to *J. Geophys. Res. Atmos.*), and Giangrande et al. (2015, manuscript submitted to *J. Geophys. Res. Atmos.*), where riming of snow was recognized by using either vertically pointing Doppler radar or in situ aircraft measurements. Vogel et al. (2015) and Giangrande et al. (2015, manuscript submitted to *J. Geophys. Res. Atmos.*) distinguish between the cases of rimed snow with unimodal and bimodal spectra of vertical Doppler velocities within the temperature interval between  $0^\circ$  and  $-10^\circ\text{C}$ . The bimodal spectra indicate secondary ice production of very anisotropic particles like needles or plates, which contribute to the increase of  $Z_{DR}$ . Vogel et al. (2015, p. 15) report that “cases with a bimodal spectra can have  $Z_{DR}$  values of about 0.2 dB up to 0.4 dB higher than non-riming cases while riming cases without a bimodal spectra can have  $Z_{DR}$  values up to 0.2 dB lower than non-riming events.” The bimodal spectra seem to be typical for the cases of weaker riming when the contribution to  $Z_{DR}$  by the primary ice with a quasi-spherical shape and highly anisotropic, smaller-size secondary ice are comparable. For heavier riming,  $Z_{DR}$  is dominated by

quasi-spherical larger-size ice, which has intrinsic  $Z_{DR}$  very close to 0 dB. Kumjian et al. (2015, manuscript submitted to *J. Geophys. Res. Atmos.*) show that heavier riming is usually associated with the “sagging bright band.”

Summarizing these latest findings, one can conclude that heavily rimed snow characterized by relatively high  $Z$  and sagging bright band has  $Z_{DR}$  very close to zero slightly above the freezing level. Dry aggregated (unrimed) snow has slightly positive  $Z_{DR}$ , which is 0.1–0.25 dB higher than heavily rimed snow. Weakly rimed

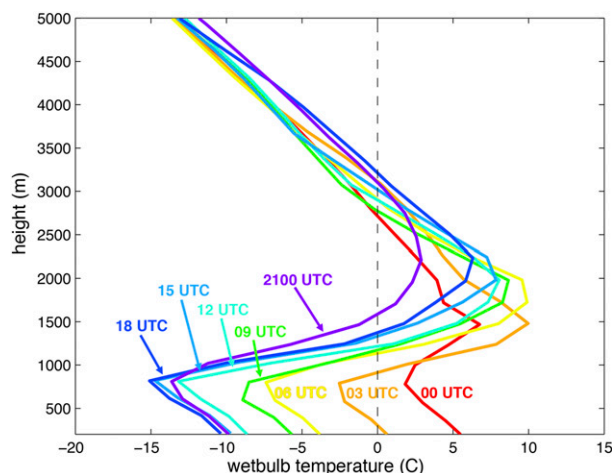


FIG. 9. Vertical profiles of the HRRR-analyzed wet-bulb temperature at KTLX from 0000–2100 UTC 2 Mar 2014: 0000, 0300, 0600, 0900, 1200, 1500, 1800, and 2100 UTC.



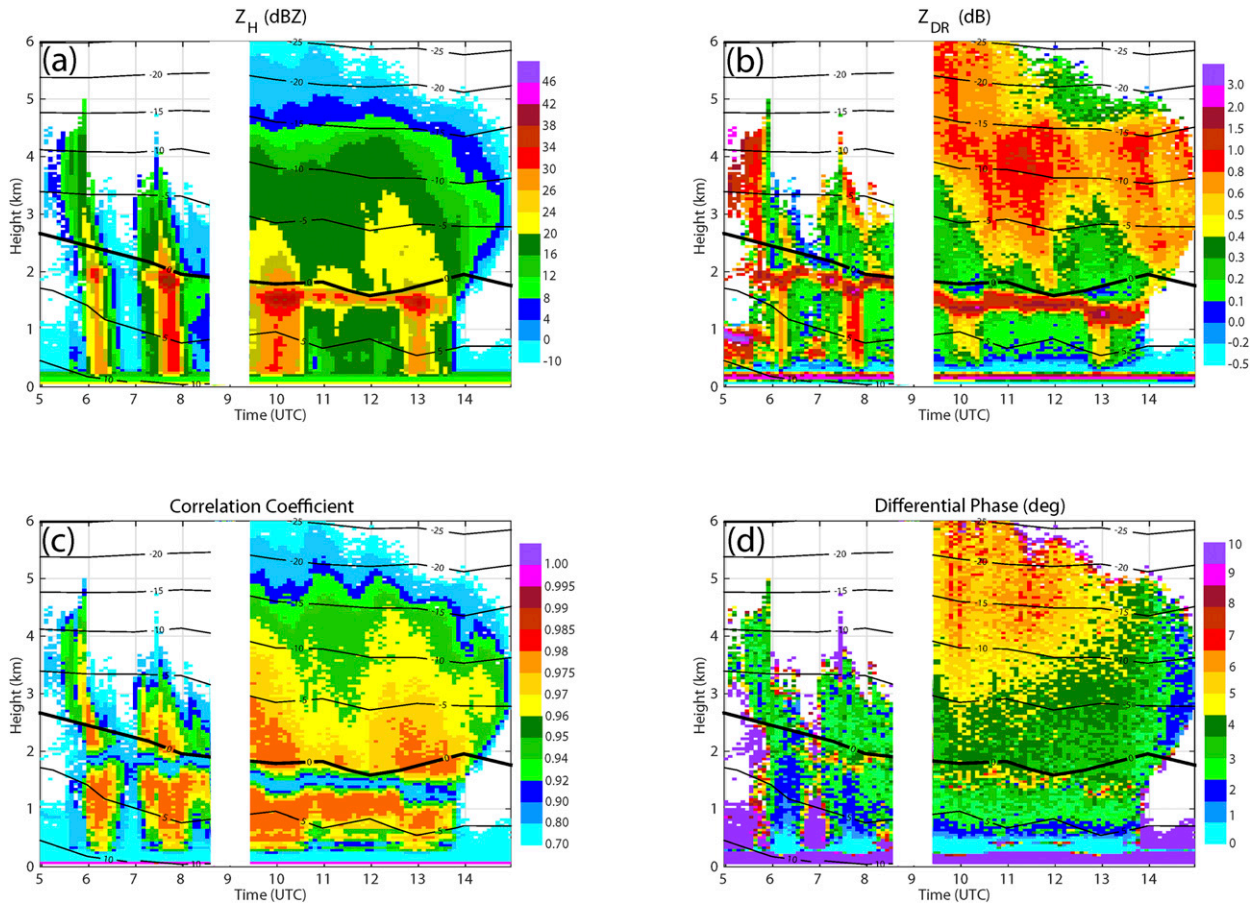


FIG. 10. As in Fig. 4, but for profiles retrieved from the research C-band ARM precipitation radar (CSAPR) data collected at elevation  $21.4^\circ$  during the storm in northern Oklahoma on 27 Apr 2011.

snow may have higher  $Z_{DR}$  than aggregated, unrimed snow if secondary ice is produced. Therefore, one can identify minimal values of  $Z_{DR}$  just above the freezing level (likely associated with heavier riming) in the QVP time series and make sure that the measured  $Z_{DR}$  is equal to zero there. Figure 8 shows that  $Z_{DR}$  measured by the KTLX WSR-88D radar above the  $0^\circ\text{C}$  level is stable and close to  $-0.5$  dB for 2 March 2014 (with minimal values of about  $-0.6$  or  $-0.7$  dB), which points to the known negative  $Z_{DR}$  bias of  $0.6$ – $0.7$  dB for this WSR-88D radar.

The QVP methodology proves to be efficient at C and X bands as well. Figure 10 shows quasi-vertical profiles of  $Z$ ,  $Z_{DR}$ , and  $\rho_{hv}$  measured by the C-band CSAPR radar in northern Oklahoma on 27 April 2011 during the MC3E field campaign. The QVP clearly exhibits two episodes of riming associated with weak embedded convection at about 0740 and 1000 UTC. All three attributes of riming are evident in the QVP plots: enhanced  $Z$ , depressed  $Z_{DR}$  above the freezing level, and downward excursion of the melting layer as indicated by  $Z_{DR}$  and  $\rho_{hv}$ . For this event, riming aloft was supported

by relatively high liquid water content at subfreezing temperatures measured on board the research aircraft and upward air motion measured by the vertically pointing 915 MHz wind profiler and Ka-band Doppler cloud radar (not shown).

Quasi-vertical profiles of polarimetric radar variables were also retrieved for a number of cases observed by the X-band dual-polarization radar at the University of Bonn, Germany (BoXPOL). One QVP example is complemented with the height–time plot of vertical Doppler velocity measured every volume scan with a vertically pointing antenna (Fig. 11). The QVP plots of  $Z$ ,  $Z_{DR}$ ,  $\Phi_{DP}$ , and  $\rho_{hv}$  with overlaid contours of temperature illustrate the features similar to those shown in the previous examples for S- and C-band radars. These include high-resolution representations of the melting layer with undulations attributed to embedded weak convection and associated riming, as well as a layer of dendritic growth aloft with strong vertical gradients of  $Z$ , increased  $Z_{DR}$ , and significant vertical gradients of  $\Phi_{DP}$ . Maximal values of  $Z_{DR}$  in the layer of dendrites do not

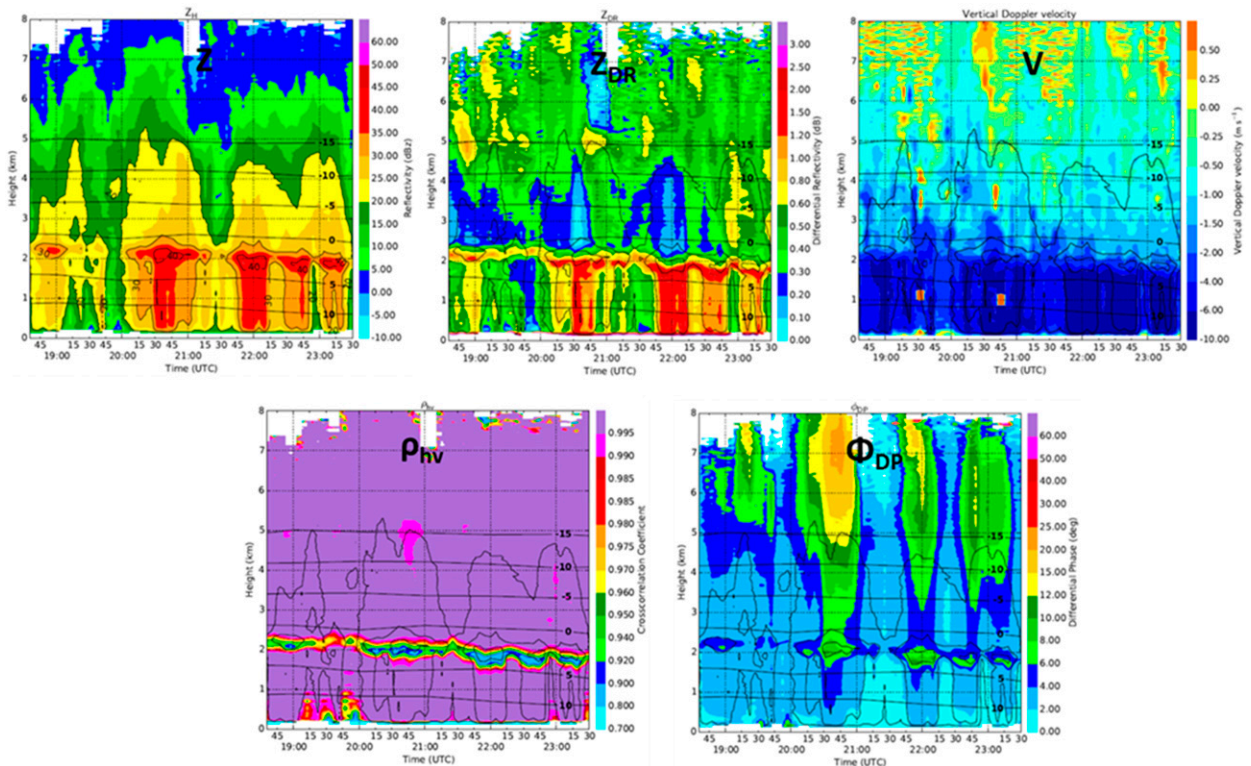


FIG. 11. The height-vs-time representation of the quasi-vertical profiles of (top) (left to right)  $Z$ ,  $Z_{DR}$ , and vertical Doppler velocity and (bottom)  $\rho_{hv}$  and  $\Phi_{DP}$ , retrieved from the data collected by BoXPol at elevation  $28^\circ$  on 6 May 2014. Overlaid are contours of  $Z$  (thin lines) and wet-bulb temperature (thick lines) retrieved from the German Meteorological Service's [Deutscher Wetterdienst (DWD)] version of the Consortium for Small-Scale Modeling (COSMO-DE) model.

exceed 1 dB in this example, implying the presence of more isotropically scattering dendrites or their aggregates compared to the case displayed in Figs. 5 and 6. The vertical gradient of  $\Phi_{DP}$  within the height interval between 3.5 and 5.3 km at about 2030 UTC corresponds to a  $K_{DP}$  of about  $1.1^\circ \text{km}^{-1}$ , which is consistent with typical  $K_{DP}$  values at X band reported by Bechini et al. (2013) and Schrom et al. (2015). The backscatter differential phase within the melting layer is notable but generally lower than the  $\delta$  measured at S band, as was previously documented by Trömel et al. (2014). The maximal value of  $\delta$  estimated in the five cases examined at X band was  $8.5^\circ$ .

Riming signatures exhibited by the sagging of the melting layer and  $Z_{DR}$  depressions in a 2-km-deep layer above the  $0^\circ\text{C}$  level are visible at about 2030 and 2200 UTC in Fig. 11. The riming signature at 2030 UTC is fairly consistent with the indication of an updraft in the vertical Doppler velocity panel at that time. A maximal updraft velocity of  $0.5 \text{ m s}^{-1}$  is measured near the cloud top between 6.5 and 7.0 km AGL. It is reasonable to assume that supercooled cloud water supported by the updraft produced riming, which could have led to an increase in the mass and density of snow particles that subsequently acquire larger terminal velocities, increasing

the magnitude of the downward Doppler velocity to  $>2 \text{ m s}^{-1}$  within the 1.5-km-deep layer above the  $0^\circ\text{C}$  level (slightly higher than 2 km AGL). This example emphasizes the importance of combining the quasi-vertical profiles of polarimetric radar variables with vertical profiles of Doppler velocities measured either by the same radar or by wind profilers or by vertically pointing cloud radars (if possible). The VAD profiles of horizontal wind or the mesoscale divergence profile obtained from the same conical scans as QVP may also contribute to the understanding of the interplay of the dynamical and microphysical processes within the clouds.

As opposed to the signal processing on the WSR-88D radars, the data obtained from the C- and X-band research radars in our study were not censored in the first range gates. Therefore, the quasi-vertical profiles of the radar variables are extended down to the surface, which is an apparent advantage for detecting low-level features.

#### 4. Summary

Several benefits of the QVP methodology are summarized herein.

- 1) The procedure for generating quasi-vertical profiles of polarimetric radar variables is very simple and straightforward, and the QVP plots in the height-versus-time format can be produced in real time for operational dual-polarization weather radars as a standard radar product.
- 2) QVP generation is an efficient way to examine the temporal evolution of microphysical processes governing precipitation production and to display physical links between polarimetric signatures aloft in the ice- or mixed-phase parts of the clouds, polarimetric characteristics of the melting layer, and the resulting rain near the surface. The method assumes horizontal uniformity of the radar echo and is particularly effective for stratiform-type precipitation. Decreasing antenna elevation degrades the vertical resolution of QVPs and increases the uncertainty associated with azimuthal averaging over larger and potentially more heterogeneous areas of the storm.
- 3) The QVP methodology facilitates an effective integration of polarimetric data obtained from the scanning surveillance weather radars with observations made by vertically pointing remote sensors such as wind profilers, lidars, radiometers, cloud radars, and radars operating at satellite or airborne platforms because the data from all these instruments can be represented in a standard height-versus-time (or height-versus-orbit/flight path) format.
- 4) The temporal evolution of the melting layer can be monitored with high vertical resolution using QVP, which presents a more reliable way to estimate  $\delta$  within the melting layer compared to standard slant angle radar scans (Trömel et al. 2013, 2014). As Trömel et al. (2014) demonstrated, measurements of  $\delta$  show good promise for estimating the maximal size of snow particles formed above the freezing level.
- 5) Another important microphysical feature aloft that can be monitored with QVP is the layer of dendritic growth. According to Kennedy and Rutledge (2011), the intensification of the layer may serve as a predictor of precipitation enhancement at the surface (snow or rain).
- 6) The height-versus-time representation of the QVP may be helpful for discrimination between snow aggregation and riming. The latter is revealed by the enhancement of  $Z$  and the decrease of  $Z_{DR}$  above the freezing level, and the subsidence of the melting layer. The difference between  $Z_{DR}$  values for aggregated snow and rimed snow with various degrees of riming is relatively small—a few tenths of a decibel—and using the QVP methodology is instrumental for detecting such small polarization contrasts.
- 7) The QVP is efficient for continuous monitoring of the absolute calibration of differential reflectivity and for detecting any other abrupt changes in the quality of the radar signal.
- 8) QVPs of polarimetric radar data can be complemented with estimates of vertical velocities or the convergence/divergence of horizontal wind from the VAD profiles obtained from the same conical radar scan and vertical velocities from collocated vertically pointing radars.

*Acknowledgments.* Funding for the study was provided by NOAA/Office of Oceanic and Atmospheric Research under NOAA–University of Oklahoma Cooperative Agreement NA11OAR4320072, U.S. Department of Commerce, and by the U.S. National Weather Service, Federal Aviation Administration, and U.S. Department of Defense program for modernization of NEXRAD radars. Additional support was given from the Grant ER65459 by the U.S. Department of Energy's Atmospheric System Research program and Grant AGS-1143948 from the U.S. National Science Foundation. Research based on the Bonn X-band radar was carried out in the framework of the Hans-Ertel-Centre for Weather Research (<http://www.herz-tb1.uni-bonn.de/>), funded by the BMVBS (Federal Ministry of Transport, Building and Urban Development), and the SFB/TR 32 (Transregional Collaborative Research Centre 32; <http://www.tr32.de/>), funded by the DFG (German Research Foundation).

## REFERENCES

- Alexander, C. R., S. S. Weygandt, T. G. Smirnova, S. Benjamin, P. Hofmann, E. P. James, and D. A. Koch, 2010: High Resolution Rapid Refresh (HRRR): Recent enhancements and evaluation during the 2010 convective season. *25th Conf. on Severe Local Storms*, Denver, CO, Amer. Meteor. Soc., 9.2 [Available online at [https://ams.confex.com/ams/25SLS/techprogram/paper\\_175722.htm](https://ams.confex.com/ams/25SLS/techprogram/paper_175722.htm).]
- Andrić, J., M. Kumjian, D. Zrnić, J. Straka, and V. Melnikov, 2013: Polarimetric signatures above the melting layer in winter storms: An observational and modeling study. *J. Appl. Meteor. Climatol.*, **52**, 682–700, doi:10.1175/JAMC-D-12-028.1.
- Bechini, R., L. Baldini, and V. Chandrasekar, 2013: Polarimetric radar observations in the ice region of precipitating clouds at C-band and X-band radar frequencies. *J. Appl. Meteor. Climatol.*, **52**, 1147–1169, doi:10.1175/JAMC-D-12-055.1.
- Giangrande, S. E., J. M. Krause, and A. V. Ryzhkov, 2008: Automatic designation of the melting layer with a polarimetric prototype of the WSR-88D radar. *J. Appl. Meteor. Climatol.*, **47**, 1354–1364, doi:10.1175/2007JAMC1634.1.
- Ice, L., J. Chrisman, J. Cunningham, W. Zittel, S. Smith, O. Boydston, R. Cook, and A. Heck, 2013: WSR-88D program data quality and efficiency enhancements—Plans and status. *36th Conf. on Radar Meteorology*, Breckenridge, CO, Amer. Meteor. Soc., 368. [Available online at <https://ams.confex.com/ams/36Radar/webprogram/Paper228782.html>.]



- Kennedy, P. C., and S. A. Rutledge, 2011: S-band dual-polarization radar observations of winter storms. *J. Appl. Meteor. Climatol.*, **50**, 844–858, doi:[10.1175/2010JAMC2558.1](https://doi.org/10.1175/2010JAMC2558.1).
- Kumjian, M. R., 2012: The impact of precipitation physical processes on the polarimetric radar variables. Ph.D. dissertation, University of Oklahoma, 328 pp.
- , A. Ryzhkov, H. Reeves, and T. Schuur, 2013: Dual-polarization radar observations of hydrometeor refreezing in winter storms. *J. Appl. Meteor. Climatol.*, **52**, 2549–2566, doi:[10.1175/JAMC-D-12-0311.1](https://doi.org/10.1175/JAMC-D-12-0311.1).
- , S. Rutledge, R. Rasmussen, P. Kennedy, and M. Dixon, 2014: High-resolution polarimetric radar observations of snow-generating cells. *J. Appl. Meteor. Climatol.*, **53**, 1636–1658, doi:[10.1175/JAMC-D-13-0312.1](https://doi.org/10.1175/JAMC-D-13-0312.1).
- Melnikov, V., 2004: Simultaneous transmission mode for the polarimetric WSR-88D. NOAA/NSSL Rep., 84 pp. [Available online at [http://cimms.ou.edu/~schuur/jpole/SHV\\_statistics.pdf](http://cimms.ou.edu/~schuur/jpole/SHV_statistics.pdf).]
- Ryzhkov, A. V., S. E. Giangrande, V. M. Melnikov, and T. J. Schuur, 2005: Calibration issues of dual-polarization radar measurements. *J. Atmos. Oceanic Technol.*, **22**, 1138–1155, doi:[10.1175/JTECH1772.1](https://doi.org/10.1175/JTECH1772.1).
- , —, A. Khain, M. Pinsky, and A. Pokrovsky, 2008: Exploring model-based polarimetric retrieval of vertical profiles of precipitation. *Extended Abstracts, Fifth European Conf. on Radar in Meteorology and Hydrology*, Helsinki, Finland, Finnish Meteorological Institute, P6.1.
- , H. Reeves, T. Schuur, M. Kumjian, and D. Zrnić, 2011: Investigations of polarimetric radar signatures in winter storms and their relation to aircraft icing and freezing rain. *35th Conf. on Radar Meteorology*, Pittsburgh, PA, Amer. Meteor. Soc., 197. [Available online at <https://ams.confex.com/ams/35Radar/webprogram/Paper191245.html>.]
- , —, J. Krause, and H. Burcham, 2014: Discrimination between winter precipitation types based on explicit microphysical modeling of melting and refreezing in the polarimetric hydrometeor classification algorithm. *Extended Abstracts, Eighth European Conf. on Radar in Meteorology and Hydrology*, Garmisch-Partenkirchen, Germany, MIC.P07. [Available online at [http://www.pa.op.dlr.de/erad2014/programme/ExtendedAbstracts/198\\_Ryzhkov.pdf](http://www.pa.op.dlr.de/erad2014/programme/ExtendedAbstracts/198_Ryzhkov.pdf).]
- Schrom, R. S., M. R. Kumjian, and Y. Lu, 2015: Polarimetric radar signatures of dendritic growth zones within Colorado winter storms. *J. Appl. Meteor. Climatol.*, **54**, 2365–2388, doi:[10.1175/JAMC-D-15-0004.1](https://doi.org/10.1175/JAMC-D-15-0004.1).
- Teshiba, M., P. Chilson, A. Ryzhkov, T. Schuur, and R. Palmer, 2009: A combined wind profiler and polarimetric weather radar method for the investigation of precipitation and vertical velocities. *J. Atmos. Oceanic Technol.*, **26**, 1940–1955, doi:[10.1175/2008JTECHA1102.1](https://doi.org/10.1175/2008JTECHA1102.1).
- Thompson, E., S. Rutledge, B. Dolan, V. Chandrasekar, and B.-L. Cheong, 2014: A dual-polarization radar hydrometeor classification algorithm for winter precipitation. *J. Atmos. Oceanic Technol.*, **31**, 1457–1481, doi:[10.1175/JTECH-D-13-00119.1](https://doi.org/10.1175/JTECH-D-13-00119.1).
- Trömel, S., M. Kumjian, A. Ryzhkov, and C. Simmer, 2013: Backscatter differential phase—Estimation and variability. *J. Appl. Meteor. Climatol.*, **52**, 2529–2548, doi:[10.1175/JAMC-D-13-0124.1](https://doi.org/10.1175/JAMC-D-13-0124.1).
- , A. Ryzhkov, P. Zhang, and C. Simmer, 2014: Investigations of backscatter differential phase in the melting layer. *J. Appl. Meteor. Climatol.*, **53**, 2344–2359, doi:[10.1175/JAMC-D-14-0050.1](https://doi.org/10.1175/JAMC-D-14-0050.1).
- Vogel, J., F. Fabry, and I. Zawadzki, 2015: Attempts to observe polarimetric signatures of riming in stratiform precipitation. *37th Conf. on Radar Meteorology*, Norman, OK, Amer. Meteor. Soc., 6B.6. [Available online at <https://ams.confex.com/ams/37RADAR/webprogram/Paper275246.html>.]
- Zawadzki, I., W. Szyrmer, C. Bell, and F. Fabry, 2005: Modeling of the melting layer. Part III: The density effect. *J. Atmos. Sci.*, **62**, 3705–3723, doi:[10.1175/JAS3563.1](https://doi.org/10.1175/JAS3563.1).